Research Article

For reprint orders, please contact: reprints@futuremedicine.com

Nanomedicine

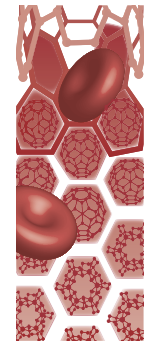

A smart drug-delivery nanosystem based on carboxylated graphene quantum dots for tumor-targeted chemotherapy

Zhen Li[‡,1], Jialong Fan[‡,1], Chunyi Tong[‡,1], Hongyan Zhou[1], Wenmiao Wang[1], Bin Li[2], Bin Liu*[,1] & Wei Wang**[,2]

[1]College of Biology, Hunan Province Key Laboratory of Plant Functional Genomics & Developmental Regulation, Hunan University, Changsha, 410082, PR China

[2]TCM & Ethnomedicine Innovation & Development International Laboratory, Innovative Materia Medica Research Institute, School of Pharmacy, Hunan University of Chinese Medicine, Changsha, 410208, PR China

*Author for correspondence: Tel.: + 86 731 8972 0939; Fax: +86 731 8972 0939; binliu2001@hotmail.com

**Author for correspondence: wangwei402@hotmail.com

‡ Authors contributed equally

Aim: Constructing a new drug-delivery system using carboxylated graphene quantum dots (cGQDs) for tumor chemotherapy *in vivo*. **Materials & methods:** A drug-delivery system was synthesized through a crosslink reaction of cGQDs, NH_2-poly(ethylene glycol)-NH_2 and folic acid. **Results:** A drug delivery system of folic acid-poly(ethylene glycol)-cGQDs was successfully constructed with ideal entrapment efficiency (97.5%) and drug-loading capacity (40.1%). Cell image indicated that the nanosystem entered into human cervical cancer cells mainly through macropinocytosis-dependent pathway. *In vivo* experiments showed the outstanding antitumor ability and low systemic toxicity of this nanodrug-delivery system. **Conclusion:** The newly developed drug-delivery system provides an important alternative for tumor therapy without causing systemic adverse effects.

First draft submitted: 6 October 2018; Accepted for publication: 12 April 2019; Published online: 29 July 2019

Keywords: antitumor • carboxylated graphene quantum dots • cGQDs • folic acid • mitoxantrone • tumor-targeted therapy

Cervical cancer is the fourth most frequent cancer and the fourth most common cause of death from cancer in women. It is estimated that more than 500,000 cases of cervical cancer occur each year, resulting in more than 250,000 annual deaths [1]. There are currently several treatment strategies used for cervical tumors, including surgery, chemotherapy, radiation therapy, immunotherapy and hormone therapy [2–5]. Among them, chemotherapy is the most common strategy, but this technique is often limited due to the poor water solubility, nonspecific selectivity, low local therapeutic concentration of drugs and adverse effects in normal cells [6–8]. Many types of nanomaterials have been adopted as drug carriers to address these limitations, including polymer nanoparticles, mesoporous silica nanoparticles, liposomes and microspheres [9–11]. Due to the mechanisms involved in the cellular uptake of nanoparticles, these carriers can effectively deliver chemotherapeutic molecules into the cytosol, nucleus or other specific intracellular sites [12]. Thus, chemical drugs with improved solubility can be delivered more efficiently into tumor cells to perform their functions. However, the therapeutic outcomes of these systems are still unsatisfactory due to the low control of release and/or poor tumor-targeted capacity of chemical drugs. Thus, enhancing the release behavior and targeting capability of chemotherapeutic drugs is an urgent necessity for developing efficient tumor therapy.

Recently, the new 2D nanomaterial graphene oxide (GO) and its derivatives have provided hopeful alternatives for constructing drug-delivery systems by using their ideal physicochemical properties, such as atomic layer structure, high dispersibility, surface area-to-volume ratio and strong capability to absorb aromatic compounds [13–15]. Along with their application to nano-biosensor construction and cell imaging [16–18], many kinds of drug-delivery systems based on GO and its derivatives have been developed through a strong π–π stacking effect and hydrogen bonds

Future Medicine

between aromatic molecules with nanomaterial since Dai first reported drug delivery by GO [19]. These nanosystems significantly improved therapeutic drug utilization by improving drug solubility and release behavior [20–24]. However, the biosafety of these nanomaterials to normal organs and tissues was not carefully considered [25]. Series toxicity studies performed by many groups, including our own, have revealed that the long-term use of pristine GO and most of its derivatives may result in DNA damage, pulmonary edema, granuloma formation, thrombus formation, neurotoxicity, and/or retardation of fetus development [26–31]. In contrast, our study of the graphene-derivative carboxylated graphene quantum dots (cGQDs) showed excellent biocompatibility and ultra-low toxicity compared with noncarboxylated GQDs or aminated GQDs [27]. Thus, this kind of nanomaterial should be considered for drug delivery due to its high biocompatibility and biosafety [32–34].

Although many studies have shown that drug delivery nanocomplexes are potential tools for efficient tumor therapy [35–37], and the heterogeneity of tumors has spurred the development of different nanocarriers for clinical therapy, the carriers' low targeting effects and the interference from patients' immune responses inevitably reduced the efficiency of these nanocomplexes. Recently, surface modification of NH_2-poly(ethylene glycol) (PEG)-NH_2 on nanomaterials improved biocompatibility, as this positive polymer reduces nonspecific protein adsorption in the blood while preventing flocculation and subsequent complement activation [38]. In addition, the amino groups of NH_2-PEG-NH_2 increase surface positive charge and structural stability in complicated surroundings [30,31], which improves cellular uptake efficiency. Considering the high and unique expression of the folate receptor (FR) on the membrane of human cervical tumor cells [39–41], dual modification of folic acid (FA) and PEG on the surface of cGQDs is a promising method to improve cell targeting capability through the FR-mediated pathway [42].

Mitoxantrone (MTN), a widely used therapeutic drug for many solid tumors including cervical cancer, has shown beneficial effects on the course of disease in cancer patients. However, potentially cumulative cardiotoxic effects including cardiomyopathy and reversible congestive heart failure were also observed [43,44]. Furthermore, the treatment efficiency of larger tumor nodules using MTN via ethanol administration is limited due to the minimal drug diffusion in tissues and excessive volume of ethanol required for tumor irradiation [45]. In order to improve the therapeutic efficacy and reduce the side effects of MTN, we constructed a smart drug delivery nanosystem for MTN using cGQDs with NH_2-PEG-NH_2 and FA modification, which showed strong antitumor capabilities *in vivo*. We believe this MTN loading system with enhanced targeting capability will facilitate successful cervical cancer therapy by improving the accumulation of MTN at tumor tissue.

Materials & methods

Construction & characterization of FA-PEG-cGQDs nanosystem

Briefly, 18 mg of N-hydroxysuccinimide and 12 mg of 1-ethyl-3-(3-dimethyl aminopropyl) carbodiimide were mixed with 5 ml cGQD (final concentration of 1 mg/ml) solution dispersed in phosphate-buffered saline (PBS) and stirred for 30 min, followed by the addition of 1 ml NH_2-PEG-NH_2 diluted with 50 mg/ml PBS, which was then stirred overnight at room temperature. Excess NH_2-PEG-NH_2 was removed using a 10 kD dialysis membrane. Finally, 6 mg FA was added in the darkness, and the solution was stirred for another 12 h. The excess FA was removed through dialyzing for 2 days [46]. The size and morphology of cGQDs and FA-PEG-cGQDs were investigated under the tapping-mode atomic force microscope (Agilent Technologies, Inc., CA, USA). The zeta potentials of cGQDs and FA-PEG-cGQDs in PBS were determined using a zeta sizer (Malvern Nano Series, Malvern, UK). The Fourier transform infrared (FT-IR) spectra of cGQDs and FA-PEG-cGQDs were recorded on a Nicolet 6700 FT-IR spectrophotometer (Thermo Fisher Scientific, Inc., MA, USA). UV–vis absorption was measured on the DU800 spectrophotometer (Beckman Coulter, Inc., CA, USA).

Loading & release of mitoxantrone

A total of 0.8 mg of MTN was mixed with 3 ml nanomaterials in the darkness and stirred for 24 h at room temperature. The obtained mixture was dialyzed using a 10 kD membrane penetration for 24 h in PBS, with fresh PBS replacement every 4 h. After collecting all filtrates into a tube, the absorbance value of the sample at 670 nm was measured. The loading capacity and encapsulation efficiency of MTN were calculated according to the following equations:

$$\mathrm{LC}\ (\%) = \frac{\mathrm{Mt} - \mathrm{Mu}}{\mathrm{Mp}} \times 100\% \qquad \text{(Eq. 1)}$$

$$EE\ (\%) = \frac{Mt - Mu}{Mt} \times 100\% \quad \text{(Eq. 2)}$$

where Mt, Mu and Mp represent the total mass of MTN, the mass of the unencapsulated MTN and the mass of the carrier cGQDs, respectively.

In order to evaluate the release of the drug, the FA-PEG-cGQDs-MTN was treated in the buffer solution with pH 5.3 or pH 7.4 for various time periods. The FA-PEG-cGQDs-MTN supernatant was then centrifugally extracted, and the MTN concentration was determined according to the corresponding fluorescence intensity.

Cellular uptake of FA-PEG-cGQDs-MTN *in vitro*

Human cervical cancer cells (HeLa) were seeded in 96-well plates at a density of 5×10^4 cells per well and cultured in a humidified 5% CO_2 incubator at 37 °C for 24 h. Then, FA-PEG-cGQDs-MTN (equivalent to an MTN concentration of 1 μg/ml) was added into each well. After incubation for 3 or 6 h, cells were washed twice with PBS. Cell nuclei stained with Hoechst 33342 for 30 min were used as the control. The intracellular uptake and localization of FA-PEG-cGQDs-MTN into HeLa cells were characterized under confocal laser scanning microscopy (CLSM; FV1200, Olympus, Tokyo, Japan).

Hemolysis assay of FA-PEG-cGQDs

The hemolysis assay was performed using fresh human blood samples obtained from the Hunan Provincial People's Hospital. A 0.9% NaCl solution and pure water were used as the negative and positive controls, respectively. Whole human blood was centrifuged at 3000 r.p.m. for 5 min and washed 5 times with PBS. Then, 0.25 ml of 4% erythrocytes (v/v) was mixed with 0.25 ml PBS containing various concentrations of FA-PEG-cGQDs or cGQDs (25, 50, 100 or 200 μg/ml) and incubated at 37 °C for 8 h. The absorbance values of the supernatants at 545 nm were measured on a microplate reader (EnSpire2300, PerkinElmer, Singapore) after centrifugation. The percentage of hemolysis was calculated using the formula below:

$$\text{Hemolysis}\ (\%) = (I/I_0) \times 100\ \% \quad \text{(Eq. 3)}$$

where I represents the supernatant absorbance value of erythrocytes with FA-PEG-cGQDs or cGQDs and I_0 represents the absorbance value of erythrocytes after complete hemolysis in pure water.

Macrophage phagocytosis study

Peritoneal macrophage cells were harvested from euthanized mice by flushing the peritoneal cavity with cold PBS and then cultured in DMEM with 10% FBS for 24 h. The cells were washed with PBS once after removing the supernatant [47]. The mixture of macrophage cells with 5 μg/ml Rhodamine B (RB)-labeled cGQDs (cGQDs-RB) or 5 μg/ml RB-labeled FA-PEG-cGQDs (FA-PEG-cGQDs-RB) was cultured for 12 h and imaged under CLSM. The quantitative assay of fluorescence intensities of macrophages with different treatments was performed using the Hitachi-F-2500 fluorescence-spectrometer (Hitachi, Tokyo, Japan).

MTT assay

Cells were seeded into 96-well plates (5000 cells per well) until adherent, and were then incubated with MTN, cGQDs-MTN or FA-PEG-cGQDs-MTN (MTN concentration was 0.05, 0.1, 0.2, 0.5 or 1 μg/ml) in serum-free medium for another 24 h. The cells with PBS treatment were considered the controls. To explore the targeting effect of FA modification, HeLa cells were treated with 10 μM free FA for 30 min before incubation with FA-PEG-cGQDs-MTN [48]. After incubation for 24 h, the medium was removed, and cells were washed with PBS three times. Then, 100 μL of 0.5 mg/ml 3-(4,5-dimethylthiazol-2-yl)-2,5-diphenyltetrazolium bromide (MTT) solution was added into the culture medium and cells were cultured for another 4 h. After carefully removing the supernatants, 150 μL dimethyl sulfoxide was added to each well. The optical density of each well at 490 nm was recorded using a microplate reader (Thermo Fisher Scientific, Inc.). The relative viability of cells was calculated using the following equation:

$$\text{Cell Viability} = \frac{OD_{490\ nm/sample}}{OD_{490nm/control}} \times 100\% \quad \text{(Eq. 4)}$$

Live/death assay & confocal laser scanning microscopy analysis

HeLa cells seeded on the coverslip were treated with MTN, FA-PEG-cGQDs-MTN, cGQDs-MTN or FA + FA-PEG-cGQDs-MTN (equivalent to 1 μg/ml MTN) for 24 h. Then, cells stained with calcein acetoxymethyl ester and propidium iodide (PI) with a final concentration of 2 μM were observed under CLSM. In addition, HeLa cells were treated with MTN, FA-PEG-cGQDs-MTN, cGQDs-MTN or FA + FA-PEG-cGQDs-MTN (equivalent to 1 μg/ml MTN) for 24 h. Then, cells were washed, harvested and co-stained with Annexin V-Alexa Fluor 488 and the PI detection kit (Sungene Biotech Co, Ltd, Tianjin, China) for detection by flow cytometry.

Animal model & biodistribution of nanocomplexes

6-week-old, athymic nude mice were subcutaneously injected with 1×10^7 HeLa cells. When the tumor volume reached 70–90 mm^3, 0.1 ml of FA-PEG-cGQDs-MTN (MTN: 2.5 mg/kg), cGQDs-MTN (MTN: 2.5 mg/kg), MTN (2.5 mg/kg) or FA-PEG-cGQDs (cGQDs: 7.56 mg/kg, based on MTN loading rate) and PBS were intravenously (iv.) administered. The therapeutic efficacy of each therapy was evaluated by measuring tumor volumes within the treatment groups over the course of 20 days. Tumor volume was measured according to the equation of $a \times b^2 \times 0.5$ every 2 days, where a and b represented the largest and the smallest dimension, respectively [49,50]. Tumors were excised at 20 days of treatment and fixed in 10% neutral formalin buffer. The sliced tumor tissues (5 μm) were stained with hematoxylin and eosin (H&E) and observed via an optical microscope. The tumor growth inhibition (TGI) rate was calculated according to the following equation:

$$\mathrm{TGI}\ (\%) = \frac{V_c - V_t}{V_c} \times 100\% \qquad \text{(Eq. 5)}$$

where V_t and V_c are the average tumor volumes of the treatment group and control group, respectively.

In order to examine the targeting properties of the nanocomplexes, the fluorescence signals of tumor-bearing mice were observed *in vivo* with a small animal, multimode imaging system (IVIS Lumina xr, MA, USA) at 12, 24 and 48 h after iv. administration of the FA-PEG-cGQDs-RB or cGQDs-RB nanocomplexes.

Western blot

HeLa cells were seeded into six-well plates with 1.2×10^6 cells/well and cultured for 24 h. Then, cells were incubated with either MTN, FA-PEG-cGQDs, FA-PEG-cGQDs-MTN, FA + FA-PEG-cGQDs-MTN or cGQDs-MTN for 24 h. Cell lyses were performed using RIPA buffer (Sigma-Aldrich, MO, USA) containing phenylmethanesulfonyl fluoride. Cell lysates were run on 10% SDS-polyacrylamide gels and transferred onto nitrocellulose membranes. After blocking with 5% skim milk in Tris-buffered saline with Tween-20, the membranes were incubated with NF-κB, IKK, Bcl-2, BAX or β-actin primary antibodies (1:500 or 1:1000 dilutions, Abcam, Inc. Massachusetts, US) overnight at 4°C, followed by incubation with HRP-conjugated secondary antibodies. The immunoreacted bands were visualized using an ECL substrate (Thermo Fisher Scientific) under a BIO-RAD ChemiDoc XRS chemiluminescence system (Bio-Rad, Inc., CA, USA). β-actin was used as an internal control.

Statistical analysis

All experiments were conducted at least in triplicate. All data are expressed as means ± standard deviations and were analyzed using one-way analysis of variance followed by Tukey's post-test. Differences with $^*p < 0.05$, $^{**}p < 0.01$ or $^{***}p < 0.001$ were considered statistically significant.

Results

Construction & characterization of FA-PEG-cGQDs-MTN

The drug loading system was synthesized as illustrated in Figure 1A. First, NH_2-PEG-NH_2 was bound to the cGQDs through the amino group at one end, and the remaining amino group was interacted with the carboxyl group of FA to form FA-PEG-cGQDs complexes. Then, FA-PEG-cGQDs nanoparticles (NPs) were used as carriers to adsorb MTN on the surface through π–π stacking and hydrogen bonds. Under the acidic tumor microenvironment, most MTN was released in the cytoplasm after internalization of FA-PEG-cGQDs-MTN into tumor cells, resulting in cell apoptosis and tumor ablation (Figure 1B).

As shown in Figure 2A, there were no obvious changes in color or aggregation of cGQDs in the different solutions after placing them at room temperature for 30 days, which reflected the high stability of the colloidal solution. The

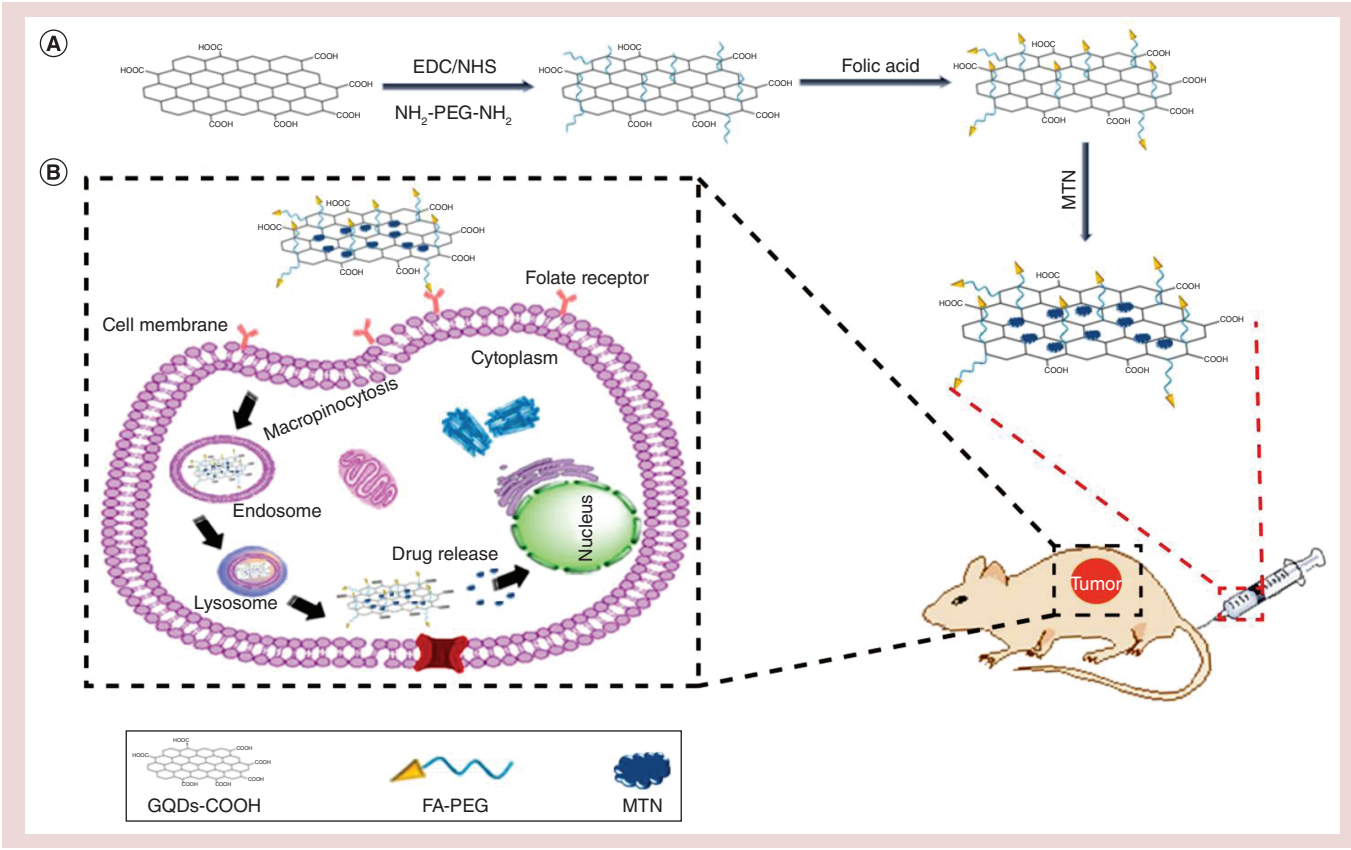

Figure 1. Folic acid-poly(ethylene glycol)-carboxylated graphene quantum dots loaded with mitoxantrone that precisely targeted anti-tumor therapy. (A) Schematic illustration of the fabrication of cGQD NPs. **(B)** Schematic illustration of FA-PEG-cGQDs-MTN NPs for tumor microenvironment responsive targeted chemotherapy of cervical tumor.
GQD: Graphene quantum dot; EDC: 1-Ethyl-3-(3-dimethylaminopropyl)carbodiimide; FA: Folic acid; MTN: Mitoxantrone; NHS: N-Hydroxysuccinimide; PEG: Poly(ethylene glycol).

zeta potential of the nanoparticles increased from -16 mV of cGQDs to 25.6 mV of FA-PEG-cGQDs NPs due to the positive charges of PEG. Moreover, the zeta potential of FA-PEG-cGQDs NPs decreased to 18.9 mV after adsorbing with MTN, a material with negative charges (Figure 2B). The FT-IR spectra indicated a decrease in the C = O absorption peak of PEG-cGQDs, FA-PEG-cGQDs and FA-PEG-cGQDs-MTN at 1850 and 1725 cm^{-1} comparing with the C=O absorption peak of bare cGQDs (Figure 2C). However, two new peak characteristics of C-H bonds appeared at 1670 and 2893 cm^{-1}, respectively. Consistent with previous reports [46], these results confirmed the successful modification of NH_2-PEG-NH_2 on the cGQDs. New peaks for MTN and FA were observed at 1570 and 3543 cm^{-1}, respectively. As depicted in Figure 2D, the transmission electron microscope image demonstrated the spherical morphology of FA-PEG-cGQDs and cGQDs NPs with a typical size of 4–10 nm, which explained their wide dispersion and stability under complicated solutions. Based on the small particle size of cGQDs, we further investigated its fluorescence properties. As shown in Supplementary Figure 1A, the maximum excitation and emission wavelength were 324 and 442 nm, respectively.

As we expected, the thickness of cGQDs increased about 0.5 nm after FA and PEG modification (Supplementary Figure 1B). The UV–vis spectrum of FA-PEG-cGQDs-MTN indicated adsorption peaks of FA and NH_2-PEG-NH_2 at 250 and 350 nm, respectively. Comparing between the peaks of FA-PEG-cGQDs, the appearance of absorption peaks at 630 and 680 nm, and the specific absorption peaks of MTN clearly demonstrated the successful modification of MTN on the FA-PEG-cGQDs (Figure 2E).

Drug release & cellular uptake of FA-PEG-cGQDs-MTN

In order to construct a high drug loading system, the optimal ratio of FA-PEG-cGQDs to MTN was investigated. The entrapment efficiency and the drug loading capacity under the optimal ratio of 1:0.8 FA-PEG-cGQDs/MTN

10.2217/nnm-2018-0378

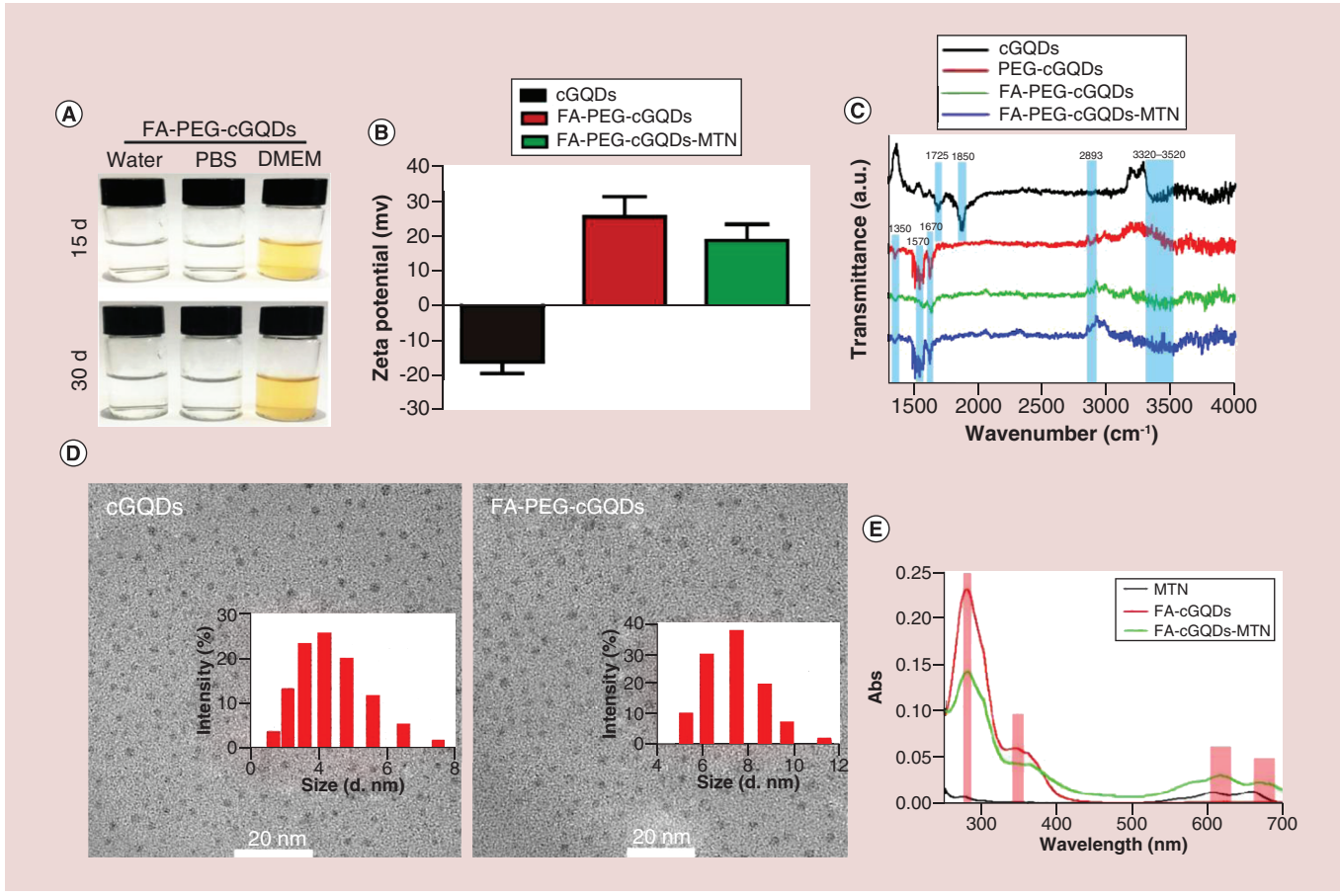

Figure 2. Characterization of folic acid-poly(ethylene glycol)-carboxylated graphene quantum dot nanoparticles. (A) Colloidal stability of FA-PEG-cGQDs in the different solutions after 30 days. **(B)** Surface zeta potentials of different samples. **(C)** Fourier transform infrared spectra of different samples. **(D)** Transmission electron microscope images of cGQDs and FA-PEG-cGQDs. **(E)** UV–vis absorbance spectra of MTN, FA-PEG-cGQDs and FA-PEG-cGQDs-MTN.
cGQD: Carboxylated graphene quantum dot; DMEM: Dulbecco`s Modified Eagle Medium; FA: Folic acid; MTN: Mitoxantrone; PBS: Phosphate-buffered saline; PEG: Poly(ethylene glycol).

were 97.5 and 40.1%, respectively (Figure 3A). The drug release rate at 37°C increased by approximately 80% compared with that at 4°C (38.3 vs 22.4%, respectively). Similarly, the release rate at pH 5.3 increased by approximately 130% compared with that at pH 7.3 (38.35 vs 16.5%, respectively) (Supplementary Figure 2B & C). The drug release behavior results of FA-PEG-cGQDs-MTN indicated a temperature- and pH-dependent MTN release from cGQDs. Consistent with previous reports [51,52], these data clearly demonstrate that both acidity and high temperature significantly promote the release of drugs.

Using RB as a fluorescence indicator, we directly investigated the cellular uptake efficiency of FA-PEG-cGQDs. FA-PEG-cGQDs-RB completely entered the cells after incubation for 3 h, and some of the nanocomplex entered into the nucleus 6 h later (Supplementary Figure 3). An inhibitor assay indicated that the cellular uptake efficiency of FA-PEG-cGQDs was deferentially reduced by the inhibitors. The uptake efficiency of tumor cells decreased more than 65% after treatment with Rottlerin, as represented by the decrease in red fluorescence signal (Figure 3B). CLSM analysis also confirmed that the intracellular red fluorescence intensity of cells treated with Rottlerin was the lowest compared with the other two inhibitor treatment groups (Supplementary Figure 4).

Biocompatibility assay

The effect of cGQDs on hemolysis was investigated to evaluate their biosafety. No significant hemolysis (less than 5%) was observed, even in the presence of 200 μg/ml cGQDs for 12 h (Figure 4A). Furthermore, the modification of FA-PEG on the cGQDs surface further reduced hemolysis to 2%. The immune evading ability of the nanocomplex

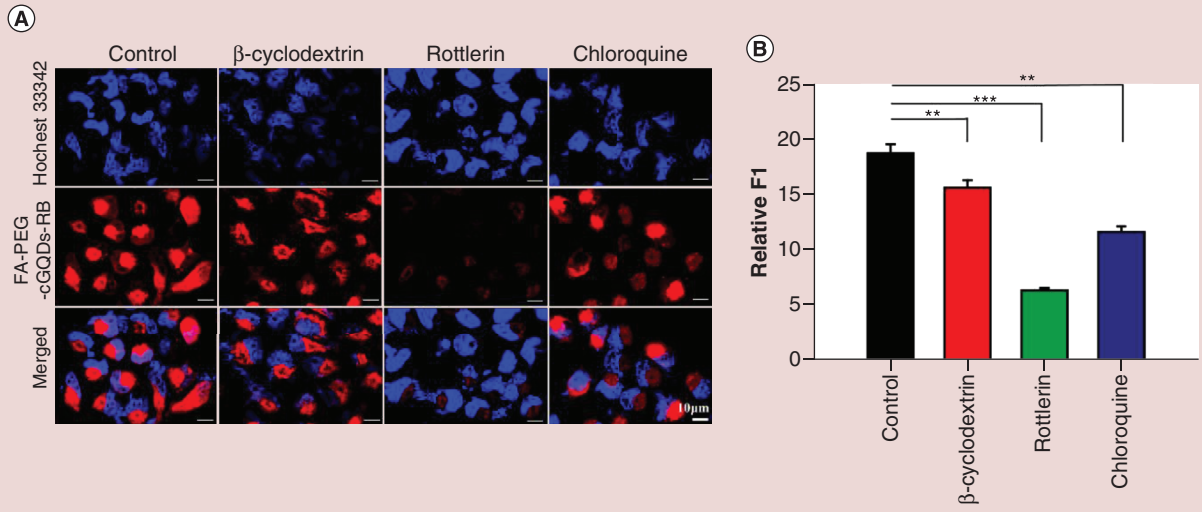

Figure 3. Cellular uptake of folic acid-poly(ethylene glycol)-carboxylated graphene quantum dots by HeLa cells. Images of cellular uptake after treatment with three types of inhibitors for 1 h under a laser scanning confocal microscope **(A)** and fluorescence quantitative analysis **(B)**.
FA: Folic acid; MTN: Mitoxantrone; PEG: Poly(ethylene glycol).

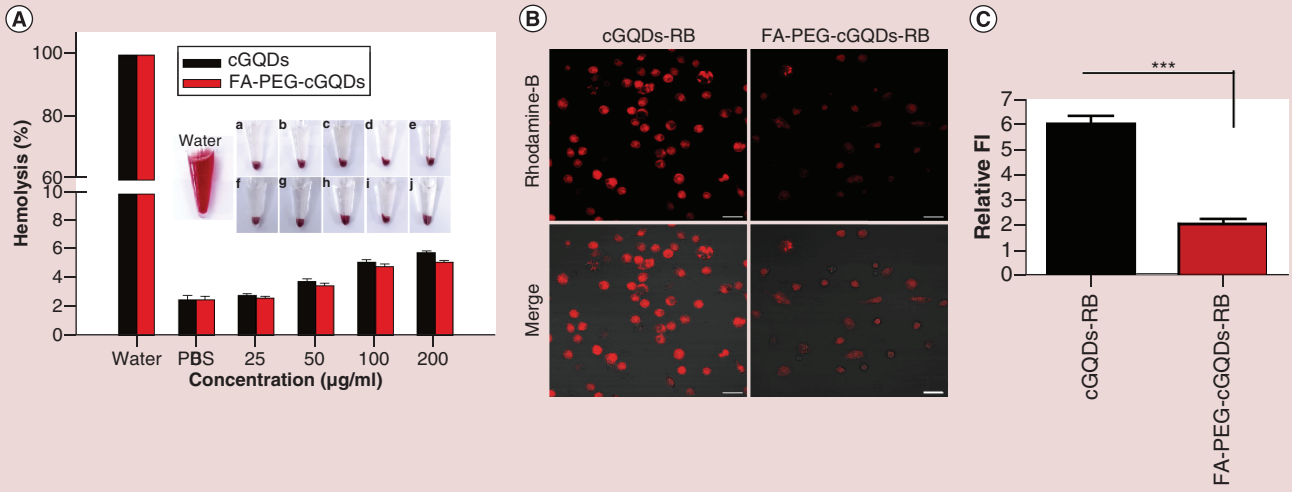

Figure 4. Representative optical photographs showing no significant hemoglobin leakage in folic acid-poly(ethylene glycol)-carboxylated graphene quantum dot-treated red blood cells comparing with the positive control (water). (A) A hemolysis assay of cGQDs (a–e) and FA-PEG-cGQDs (f–j) at different concentrations (0–200 μg/ml) of whole blood treated with water, phosphate-buffered saline, FA-PEG-cGQDs or cGQDs was quantified using a fluorimeter. **(B)** Phagocytic cellular uptake of FA-PEG-cGQDs-RB and cGQDs-RB for 4 h. The scale bar is 20 μm. **(C)** The FI for phagocytic cells after uptake of FA-PEG-cGQDs and cGQDs.
cGQD: Carboxylated graphene quantum dot; FA: Folic acid; FI: Fluorescence intensity; PBS: Phosphate-buffered saline; PEG: Poly(ethylene glycol); RB: Rhodamine B.

was then investigated by incubating FA-PEG-cGQDs with macrophages. Although most macrophages emitted strong red fluorescence following incubation with cGQDs-RB, only a few macrophages emitted red fluorescence after incubation with FA-PEG-cGQDs-RB (Figure 4B). A quantitative assay of fluorescence signal further illustrated that the modification of FA-PEG on cGQDs resulted in more than a 66% reduction in phagocytosis (Figure 4C). The MTT assay also indicated that no toxic effects were observed when either HeLa or MDA-MB-231 cells were treated with FA-PEG-cGQDs for 24 h. Furthermore, more than 95% cell viability was attained, even with a high

10.2217/nnm-2018-0378

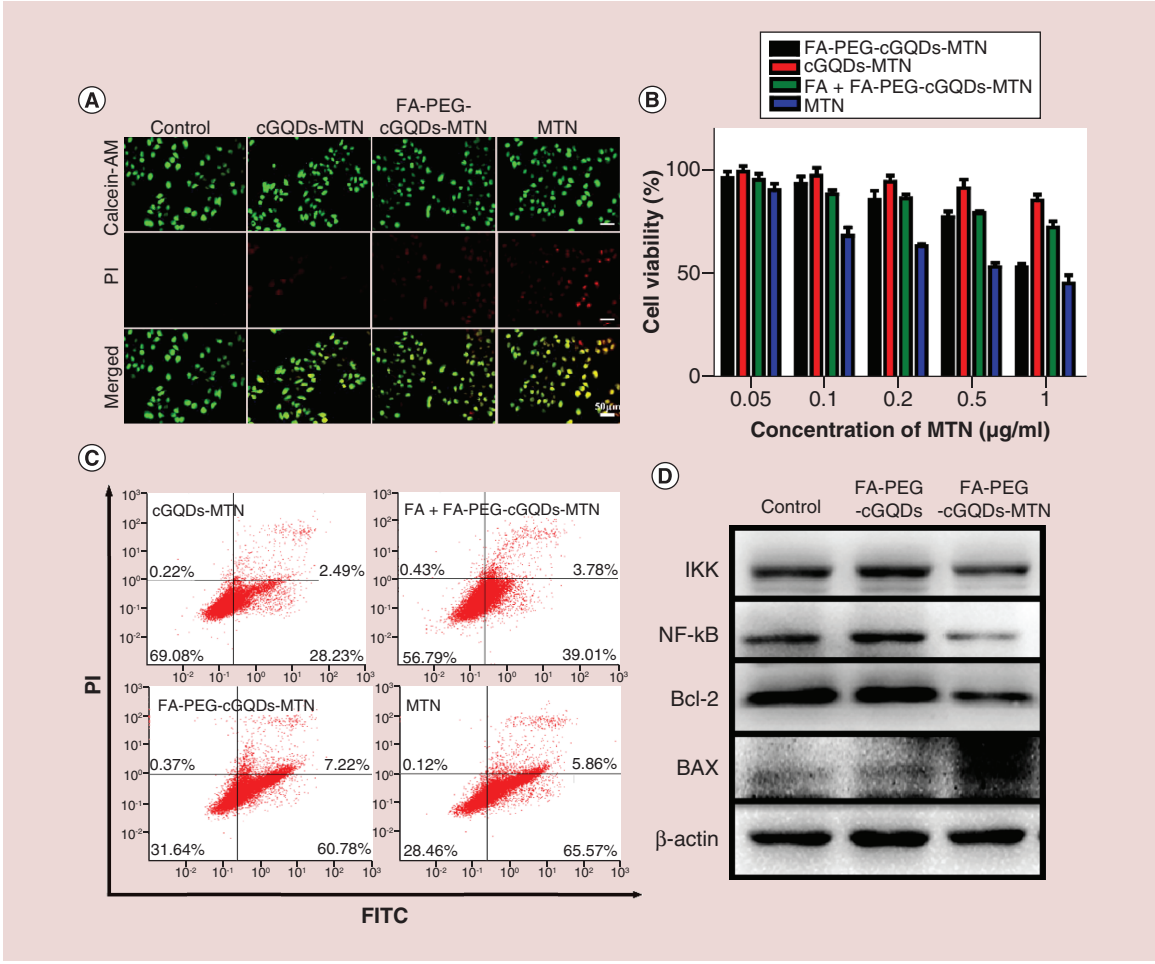

Figure 5. ***In vitro*** **anticancer performance. (A)** Live/dead staining of tumor cells after incubation with cGQDs-MTN, FA-PEG-cGQDs-MTN and FA + FA-PEG-cGQDs for 12 and 24 h. Live cells are depicted as green and dead cells are depicted as red. **(B)** Relative cell viability of HeLa cells after treatment with FA-PEG-GQDs-MTN, GQDs-MTN, FA + FA-PEG-cGQDs-MTN or MTN with different concentrations for 24 h. **(C)** Flow cytometry assays of HeLa Cells treated with cGQDs-MTN, FA + FA-PEG-cGQDs-MTN, FA-PEG-cGQDs-MTN or MTN. **(D)** Western blot analysis of the proteins in HeLa cells after various treatments for 48 h.
cGQD: Carboxylated graphene quantum dot; FA: Folic acid; HeLa: Human cervical cancer cell; MTN: Mitoxantrone; PEG: Poly(ethylene glycol).

concentration treatment of 200 μg/ml FA-PEG-cGQDs (Supplementary Figure 5). These data demonstrate that FA-PEG modification can efficiently decrease the phagocytosis of FA-PEG-cGQDs by macrophages, which may increase circulation time and reduce immune response for *in vivo* experiments.

In vitro antitumor therapy

The results of calcein acetoxymethyl ester and PI staining showed the stronger cell-killing capability of FA-PEG-cGQDs-MTN compared with its analog, which was represented by the strong red fluorescence in the FA-PEG-cGQDs-MTN treatment group (Figure 5A). The MTT assay also showed that the relative viability of HeLa cells with FA-PEG-cGQDs-MTN treatment decreased compared with those treated with cGQDs-MTN (52.9 vs 85%) (Figure 5B). It should be noted that the killing efficiency of FA-PEG-cGQDs-MTN for tumor cells was reduced by approximately 7% relative to the bare MTN treatment group (45.8%). Considering these results along with the data in Supplementary Figure 2B, we suspect that the increase in cell viability was mainly caused by the gradual release of MTN from FA-PEG-cGQDs. In addition, the FACS analysis depicted in Figure 5C indicated that the apoptosis rates of the cGQDs-MTN, FA-PEG-cGQDs-MTN and MTN treatment groups were 39.01, 60.78, and 65.57%, respectively. These results reflect the improved cancer cell-killing ability of FA-PEG-cGQDs-MTN compared

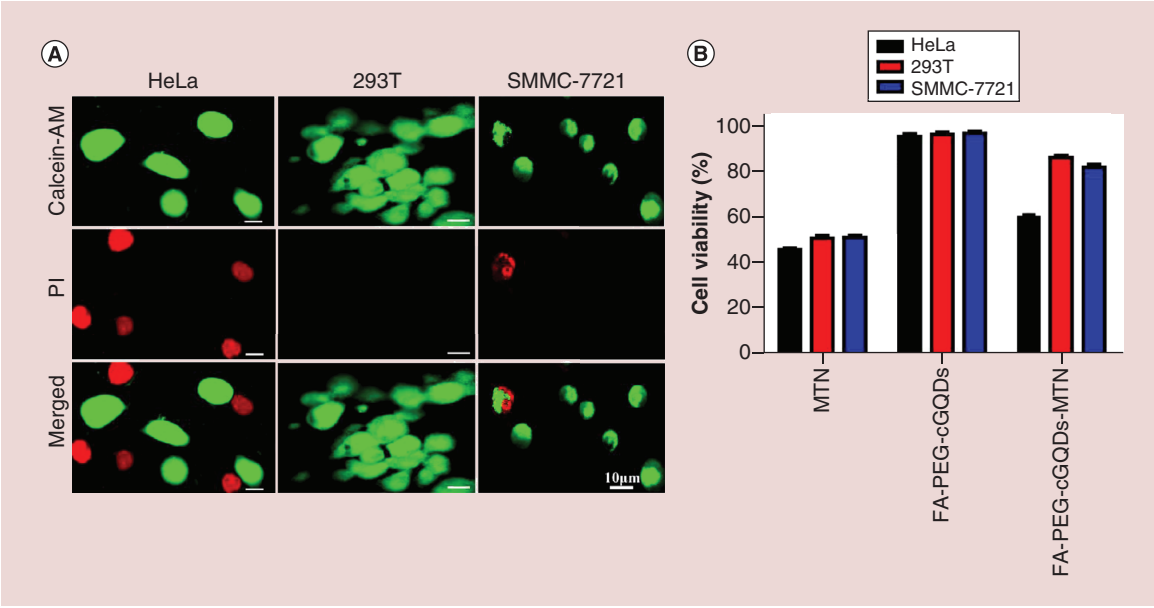

Figure 6. Folate receptor expression level assay. (A) Confocal fluorescence images of HeLa, SMMC-7721 and 293-T cells after incubating with FA-PEG-cGQDs-MTN for 24 h. Scale bar is 10 μm. **(B)** Growth inhibition assay (MTT) of HeLa, 293-T and SMMC-7721 cells after incubating with MTN, FA-PEG-cGQDs, FA-PEG-cGQDs-MTN for 24 h.
FA: Folic acid; HeLa: Human cervical cancer cell; MTN: Mitoxantrone; PEG: Poly(ethylene glycol); PI: Propidium Iodide.

with cGQDs-MTN. Further detection of apoptosis-related protein levels using western blot demonstrated that the level of BAX in HeLa cells was significantly upregulated, whereas Bcl-2 was inhibited after FA-PEG-cGQDs-MTN treatment. Meanwhile, IKK and NF-κB expressions were inhibited after FA-PEG-cGQDs-MTN treatment (Figure 5D). These results demonstrate that cell apoptosis induction occurs mainly through the *Bcl-2* pathway.

In addition, we investigated the effect of FR on the cell-killing capability of FA-PEG-cGQDs-MTN. Three types of cell lines were selected. HeLa cells showed high expression of FR, human hepatoma cells SMMC-7721 showed low expression of FR while no FR was expressed on 293T cells. The live/dead staining results indicated that the number of cells with red fluorescence signals decreased according to the sequence of HeLa, SMMC-7721 and 293T cells. Almost no 293T cells emitted red fluorescence (Figure 6A). The survival rates of cells following FA-PEG-cGQDs-MTN treatment were 58, 86.2, and 86.2% for HeLa, 293T and SMMC-7721 cells, respectively (Figure 6B). The survival rates of these cell lines were about 95% after treatment with FA-PEG-cGQDs for 24 h, which demonstrated the ultra-low cytotoxicity of this nanomaterial.

In vivo biodistribution

In order to explore the targeting capability of FA-PEG-cGQD-MTN *in vivo*, RB was used as an indicator for real-time monitoring the distribution of nanomaterials *in vivo*. Figure 7A showed the random distribution of cGQDs-MTN-RB in the whole body with weak accumulation at the tumor site after intravenous administration for 12 h. Then, the fluorescence signal gradually centered on the area around the liver. In contrary, the fluorescence signal at the tumor site decreased gradually after 48 h. However, most of FA-PEG-cGQDs-MTN accumulated at the tumor site after intravenous administration for 12 h, which was reflected by the strong fluorescence signal at the tumor site. The fluorescence signal distributed in other parts gradually disappeared as the time extended. However, a strong fluorescence signal was still observed at the tumor site after 48 h. By investigating the distribution of FA-PEG-cGQDs-MTN in different organs after intravenous administration for 48 h, it was found that the fluorescence signal was mainly located at the tumor site. As a control, cGQDs-MTN was mainly distributed in the liver, lungs and kidneys, but not the tumor tissue (Figure 7B & C).

In vivo antitumor therapy experiment & tissue section analysis

Encouraged by the outstanding biocompatibility, high cell-killing efficiency and targeting ability of FA-PEG-cGQDs-MTN *in vitro*, we then investigated the effect of its administration on bodyweight and antitumor ability in

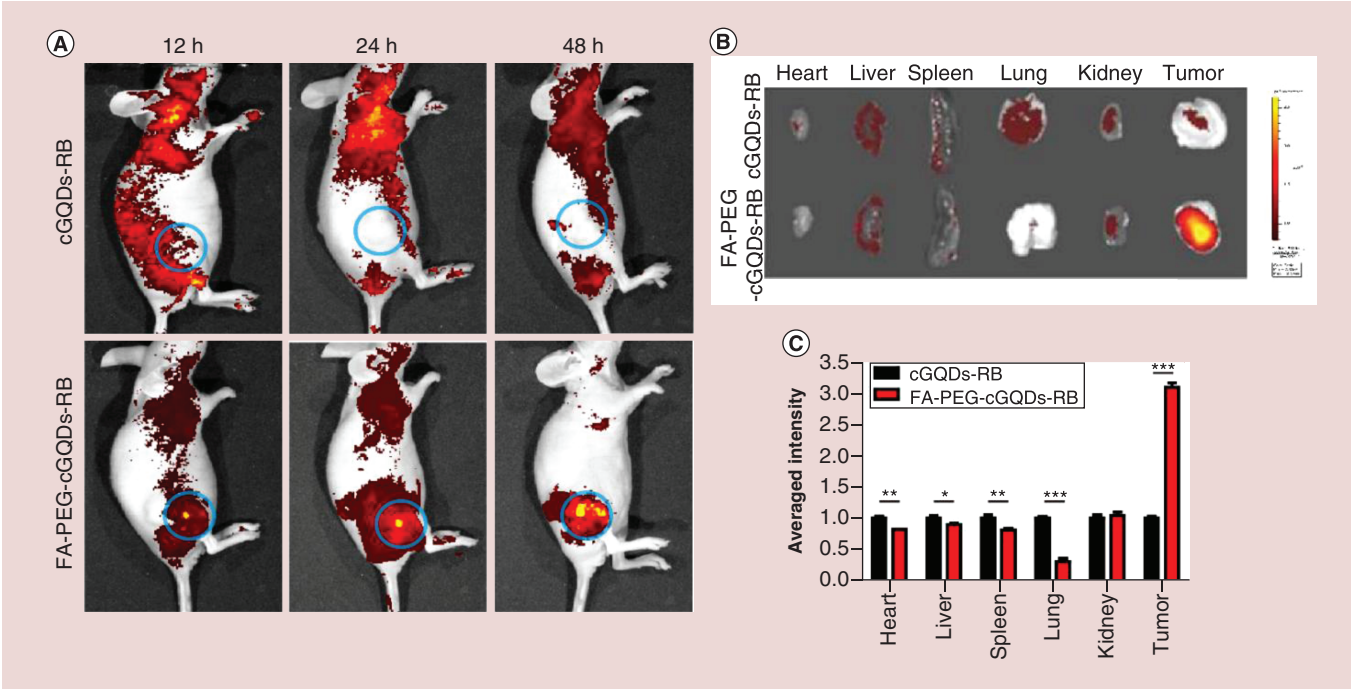

Figure 7. *In vivo* imaging and biodistribution analysis of cervical tumor-bearing nude mice after injection of carboxylated graphene quantum dots-rhodamine B and folic acid-PEG-carboxylated graphene quantum dots-rhodamine B. **(A)** Time-dependent fluorescence imaging of FA-PEG-cGQDs-RB and cGQDs-RB in the cervical tumor-bearing mice (the tumors indicated by a blue circle). **(B)** Near-infrared fluorescence images of major organs and tumors after 48 h postinjection of cGQDs-RB and FA-PEG-cGQDs-RB. **(C)** Semi-quantitative assay of cGQDs-RB and FA-PEG-cGQDs-RB signal in the cervical tumor bearing nude mice determined from the average fluorescence intensity of each organ.
cGQD: Carboxylated graphene quantum dot; FA: Folic acid; PEG: Poly(ethylene glycol); RB: Rhodamine B.

tumor-bearing mice (Supplementary Figure 6 & Figure 8). No mice in all investigated groups displayed an obvious decrease in bodyweight after 18 days of treatment, besides some weak fluctuations (Figure 8A). However, the curves of the tumor growth varied dramatically between treatment groups. The sizes of tumors treated with FA-PEG-cGQDs-MTN were the smallest of all groups (Figure 8C). Compared with the PBS control group, cGQDs-MTN and MTN inhibited tumor growth with a TGI rate of 72 and 71.8%, respectively, due to the passive targeted effect [53]. Meanwhile, the TGI rate of the FA-PEG-cGQDs-MTN treatment group was approximately 99.68% (Figure 8B). Histological analyses indicated programmed cell necrosis in most tumor tissue (Figure 8D). In order to further explore the side effects *in vivo*, the major organs of tumor-bearing nude mice were removed for sectioning and staining with H&E. There was no off-target damage to normal tissues observed in the mice after treatment with FA-PEG-cGQDs-MTN for 20 days (Supplementary Figure 7).

Discussion

This study introduced a smart drug delivery nanosystem comprised of cGQDs grafted with PEG and FA for cervical tumor therapy. Undoubtedly, cGQDs with high biocompatibility of uniform and small sizes provide an ideal alternative for MTN loading. Furthermore, the convenient addition of NH_2-PEG-NH_2 to the surface of cGQDs significantly improved the stability and prevented aggregation of the nanodrugs. Moreover, covalent modifications by PEG and FA efficiently adjust the surface potential of the cGQDs to meet the requirements of drug delivery. These advantageous alterations decreased the amount of cGQDs, the concentration of MTN and uptake time required to realize efficient tumor therapy. In addition, previous studies confirmed the overexpression of FA receptor on cancer cells, especially HeLa cells, which may enhance the targeting effects of drug-delivery systems for tumor therapy [33]. Our results also confirmed that the modification of FA significantly improved the local drug concentration and cellular uptake efficiency, which is consistent with previous reports [51]. For this reason, we suspect that the specific interaction of FA with its receptor maximized their binding affinity to reduce steric hindrance toward the cell receptor and decreased nonspecific internalization of the nanocomplex into other

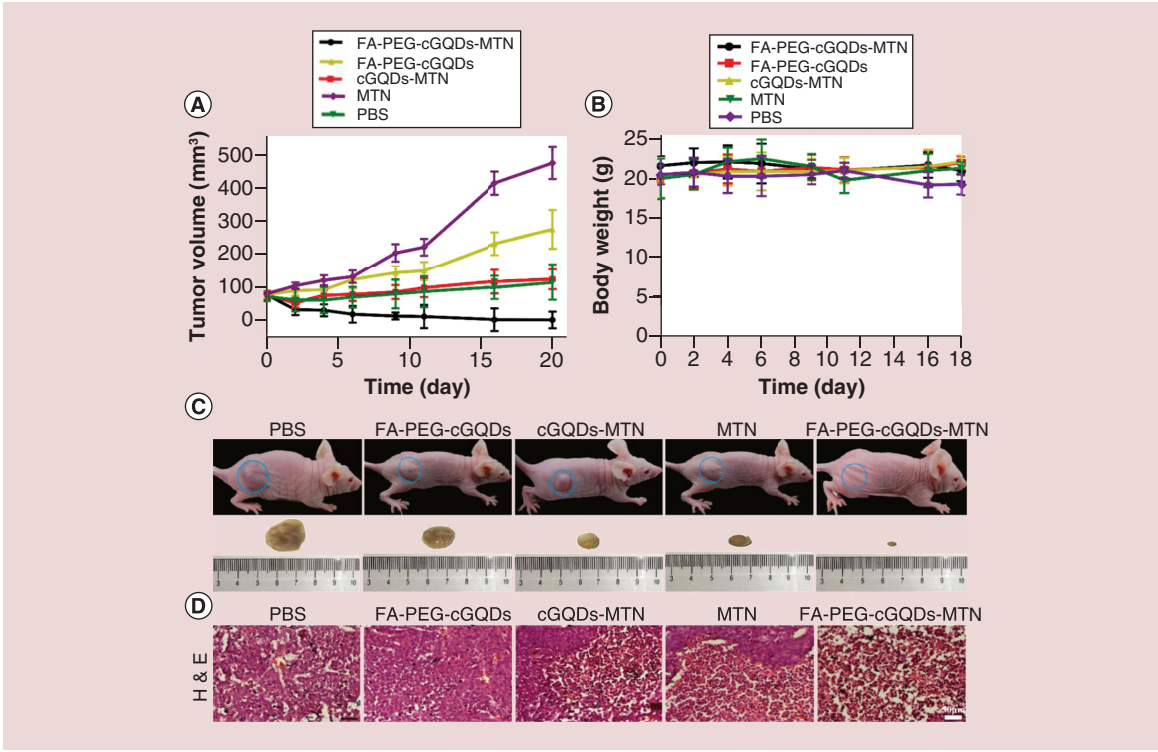

Figure 8. ***In vivo*** **study of folic acid-poly(ethylene glycol)-carboxylated graphene quantum dot-mitoxantronein anti-tumor therapy. (A)** The weight curves of cervical tumor-bearing nude mice. **(B)** Tumor growth curves of different groups with different treatments. Each data point is the mean + standard deviation (n = 3 mice per group). **(C)** Representative photos of cervical tumor-bearing nude mice at day 20. The tumors marked with a dashed circle were excised after treatment for 20 days. **(D)** H&E-stained images of the excised tumor tissue with different treatments. cGQD: Carboxylated graphene quantum dot; FA: Folic acid; H&E: Hematoxylin and eosin; HeLa: Human cervical cancer cell; MTN: Mitoxantrone; PBS: Phosphate-buffered saline; PEG: Poly(ethylene glycol).

normal cells. In addition to this FA/FR mechanism, the tight π–π interaction between the cGQDs and MTN is beneficial for cellular uptake. The results of this study clearly indicated that the uptake of targeted drugs by HeLa cells was more efficient than normal cells, which aids the performance of its high antitumor function.

Furthermore, *in vitro* and *in vivo* results of the study clearly indicated the high delivery efficiency of FA-PEG-cGQDs-MTN compared with the PEG-cGQDs-MTN, cGQDs-MTN and MTN analogs. Fluorescence images of CLSM also revealed a rapid internalization of targeted nanocomplexes into the cytosol. Meanwhile, the control experiments indicated that the pretreatment of HeLa cells with FA could retard the cellular entry of chemical drugs. Thus, we suspect that the electrostatic interactions between the phosphate groups of the cellular membrane with FA-PEG-cGQDs-MTN and FA facilitates nucleation and provides transient pores in the lipid bilayer through cell-penetrating peptide pathways, which are beneficial for delivering MTN into tumor cells [54].

It has been reported that pristine GO and its derivative of reduced GO exhibited significant toxicity to normal and tumor cells at dosages more than 30 μg/ml. [23] In the present study, no cellular toxicity was observed even when 200 μg/ml cGQDs was used as the drug carrier (Figure 4 & Supplementary Data). These data are valuable evidence supporting our selection of cGQDs as a drug carrier. In addition, many studies have reported that FA modification improves the cellular internalization and increases cellular toxicity of drugs. These studies also indicated that targeted drug carriers were more accumulated into the target cells compared with other nontargeted drugs [42]. Similar results were obtained in this study, in that FA-PEG-cGQDs-MTN displayed the highest uptake efficiency and tumor cell-killing ability compared with other nontargeted analogs. The strong tumor cell-killing ability of FA-PEG-cGQDs-MTN could be attributed to higher internalization of targeted nanocarriers and higher levels of MTN entering into cancer cells (Figure 3). In addition, the shorter period of time required for endocytosis with the help of a cell membrane receptor should be considered. Moreover, the drug system efficiently induced tumor cell apoptosis through the *Bcl-2* pathway, which is consistent with previous reports [55].

10.2217/nnm-2018-0378

In vivo studies showed a significant targeted effect of FA-PEG-cGQDs-MTN and a higher accumulation capability at tumor sites in comparison with other analogs. In contrary, cGQDs-MTN was mainly distributed in the liver, lungs and kidneys. Only a weak fluorescence signal was observed in the tumor tissue (Figure 7B & C). These results confirmed that FA modification significantly improves the targeted effects of chemical drugs, which is the key to improving their therapeutic efficacy and reducing side effects. FA-PEG-cGQDs-MTN treatment of tumor-bearing mice also resulted in the inhibition of tumor growth at a TGI rate of 99.68% (Figure 8B), whereas treatment with cGQDs-MTN and MTN only inhibited tumor growth at a TGI rate of 72 and 71.8%, respectively, due to the passive targeted effect [53]. More importantly, the results of H&E staining indicated that the major organs of tumor-bearing mice did not exhibit off-target damage to normal tissues, which further confirms the advantage of the high target specificity of FA-PEG-cGQDs-MTN *in vivo* (Supplementary Figure 7). This particular characteristic is the most urgent motivator for the application of this smart system to clinical therapy.

In conclusion, FA-PEG-cGQDs-MTN nanocomplexes with high stability, high affinity and uniform size were synthesized in our work. The nanocomplexes showed enhanced biocompatibility and immune evasion due to the FA-PEG modification. Furthermore, this controlled-release drug system showed a significant targeted killing capability for HeLa cells with high FR expression. The *in vivo* experiments further indicated that high accumulation of FA-PEG-cGQDs-MTN at tumorigenic regions might result in superior antitumor outcomes without obvious toxicities or side effects in normal tissues. Thus, our results suggest that this nanomaterial can be widely applied for clinical tumor therapy. Although we have developed an efficient alternative method for chemotherapy in tumor-bearing mice, the future application of this method in clinical settings should be carefully considered by using clinical tumor models to more accurately evaluate its biosafety and efficiency. Furthermore, its immune evasion capabilities should be improved by using mimetic membranes in future research.

Summary points

- Carboxylated graphene quantum dots (cGQDs) with high biocompatibility and thin and small sizes may support the mitoxantrone structure much better than other materials.
- Decorating the surface of cGQDs with NH_2-PEG-NH_2 significantly improved the stability and prevented aggregation of the nanodrugs.
- Surface modification of folic acid (FA) and poly(ethene glycol; PEG) increased the loading of mitoxantrone and protected them from clearance during delivery to the target position.
- FA-PEG modification efficiently decreased phagocytosis by macrophages, which increases circulation time and reduces the immune response.
- Modification of FA-PEG in cGQDs surface-based nanoparticles provides an opportunity to intelligently design targeted therapies for specific tumors by changing the targeting molecules.

Supplementary data

To view the supplementary data that accompany this paper please visit the journal website at: www.futuremedicine.com/doi/full/10.2217/nnm-2018-0378

Acknowledgments

The authors cordially thank F Xiao for his help in data processing.

Financial & competing interests disclosure

This work was partially supported by the National Natural Science Foundation of China (grant nos: 81874369 and 81673579), Ministry of Science and Technology of PR China (grant no.: 2018FY100703) and Hunan Science and Technology Department (grant nos: 2019JJ50315, 2018SK 2110 and 2081). The authors have no other relevant affiliations or financial involvement with any organization or entity with a financial interest in or financial conflict with the subject matter or materials discussed in the manuscript apart from those disclosed.

Funding writing assistance has been utilized; this manuscript has been edited by a native English professor from Enago, the editing company used by Crimson Interactive Consulting Co. Ltd.

Ethical conduct of research

The authors state that they have obtained appropriate institutional review board approval or have followed the principles outlined in the Declaration of Helsinki for all human or animal experimental investigations.

References

Papers of special note have been highlighted as: • of interest; •• of considerable interest

1. Luo J, Solimini NL, Elledge SJ. Principles of cancer therapy: oncogene and non-oncogene addiction. *Cell* 136, 823–837 (2009).
2. Lammers T, Aime S, Hennink WE *et al.* Theranostic nanomedicine. *Acc. Chem. Res.* 44, 1029–1038 (2011).
3. Postow MA, Callahan MK, Wolchok JD. Immune checkpoint blockade in cancer therapy. *JCO* 33, 1974–1982 (2015).
4. Morton SW, Lee MJ, Deng ZJ *et al.* A nanoparticle-based combination chemotherapy delivery system for enhanced tumor killing by dynamic rewiring of signaling pathways. *Sci. Signal.* 7, ra44 (2014).
5. Topalian SL, Taube JM, Anders RA *et al.* Mechanism-driven biomarkers to guide immune checkpoint blockade in cancer therapy. *Nat. Rev. Cancer* 16, 275–287 (2016).
6. Botchkarev VA, Sharov AA. Modeling chemotherapy-induced hair loss: from experimental propositions toward clinical reality. *J. Invest. Dermatol.* 136, 557–559 (2016).
7. Wicki A, Witzigmann D, Balasubramanian V *et al.* Nanomedicine in cancer therapy: challenges, opportunities, and clinical applications. *J. Control. Rel.* 200, 138–157 (2015).
8. Liu J, Detrembleur C, De Pauw-Gillet MC *et al.* Gold nanorods coated with mesoporous silica shell as drug delivery system for remote near infrared light-activated release and potential phototherapy. *Small* 11, 2323–2332 (2015).
9. Cheng CJ, Bahal R, Babar IA *et al.* MicroRNA silencing for cancer therapy targeted to the tumour microenvironment. *Nature* 518, 107–110 (2015).
10. Xu Z, Zhu S, Wang M, *et al.* Delivery of paclitaxel using pegylated graphene oxide as a nanocarrier. *ACS Appl. Mater. Interfaces* 7, 1355–1363 (2015).
11. Chung C, Kim YK, Shin D *et al.* Biomedical applications of graphene and graphene oxide. *Acc. Chem. Res.* 46, 2211–2224 (2013).
12. Behzadi S, Serpooshan V, Tao W *et al.* Cellular uptake of nanoparticles: journey inside the cell. *Chem. Soc. Rev.* 46, 4218–4244 (2017).
13. Wu D, Zhang F, Liang H *et al.* Nanocomposites and macroscopic materials: assembly of chemically modified graphene sheets. *Chem. Soc. Rev.* 41, 6160–6177 (2012).
14. Ji H, Zhang L, Pettes MT *et al.* Ultrathin graphite foam: a three-dimensional conductive network for battery electrodes. *Nano Lett.* 12, 2446–2451 (2012).
15. Ahn G, Kim HR, Ko TY *et al.* Optical probing of the electronic interaction between graphene and hexagonal boron nitride. *ACS Nano* 7, 1533–1541 (2013).
16. Yang K, Gong H, Shi X *et al. In vivo* biodistribution and toxicology of functionalized nano-graphene oxide in mice after oral and intraperitoneal administration. *Biomaterials* 34, 2787–2795 (2013).
17. Jaworski S, Sawosz E, Kutwin M *et al. In vitro* and *in vivo* effects of graphene oxide and reduced graphene oxide on glioblastoma. *Int. J. Nanomater.* 10, 1585–1596 (2015).
18. Fan JL, Zhang XZ, Cheng YX *et al.* Increasing the sensitivity and selectivity of a GONS quenched probe for an mRNA assay assisted with duplex specific nuclease. *RSC Adv.* 7, 35629–35637 (2017).
19. Liu Z, Robinson JT, Sun X *et al.* PEGylated nanographene oxide for delivery of water-insoluble cancer drugs. *J. Am. Chem. Soc.* 130, 10876–10877 (2008).
20. Yang LC, Zhong XY, Li Q *et al.* Potentiation of drug induced phospholipidosis in vitro through PEGlyated graphene oxide as the nanocarrier. *Toxicol. Sci.* 156, 39–53 (2017).
21. Wang Y, Polavarapu L, Liz-Marzán LM. Reduced graphene oxide-supported gold nanostars for improved SERS sensing and drug delivery. *ACS Appl. Mater. Interfaces* 6, 21798–21805 (2014).
22. Miao W, Shim G, Kang CM *et al.* Cholesteryl hyaluronic acid-coated, reduced graphene oxide nanosheets for anti-cancer drug delivery. *Biomaterials* 34, 9638–9647 (2013).
23. Weaver CL, Larosa JM, Luo X *et al.* Electrically controlled drug delivery from graphene oxide nanocomposite films. *ACS Nano* 8, 1834–1843 (2014).
24. Shim G, Kim JY, Han J *et al.* Reduced graphene oxide nanosheets coated with an anti-angiogenic anticancer low-molecular-weight heparin derivative for delivery of anticancer drugs. *J. Control. Rel.* 189, 80–89 (2014).
25. Cheng C, Li S, Thomas A *et al.* Functional graphene nanomaterials based architectures: biointeractions, fabrications, and emerging biological applications. *Chem. Rev.* 117, 1826–1914 (2017).
26. Iannazzo D, Pistone A, Salamò M *et al.* Graphene quantum dots for cancer targeted drug delivery. *Int. J. Pharm.* 518, 185–192 (2017).

27. Li J, Zhang X, Jiang J *et al.* Systematic assessment of the toxicity and potential mechanism of graphene derivatives *in vitro* and *in vivo*. *Toxicol. Sci.* 167, 269–281 (2019).

•• **First systematic study of the toxicity and potential mechanism of graphene derivatives *in vitro* and *in vivo*, which indicated that carboxylated graphene quantum dots have excellent biological compatibility and ultra-low-toxicity.**

28. Ma Y, Shen H, Tu X *et al.* Assessing *in vivo* toxicity of graphene materials: current methods and future outlook. *Nanomedicine* 9, 1565–1580 (2014).

29. Li Y, Wan J, Zhang Z *et al.* Targeted soft biodegradable glycine/PEG/RGD-Modified poly (methacrylic acid) nanobubbles as intelligent theranostic vehicles for drug delivery. *ACS Appl. Mater. Interfaces* 9, 35604–35612 (2017).

30. Bi C, Wang A, Chu Y *et al.* Intranasal delivery of Rotigotine to the brain with lactoferrin-modified PEG-PLGA nanoparticles for Parkinson's disease treatment. *Int. J. Nanomater.* 11, 6547–6559 (2016).

31. Chao X, Guo L, Zhao Y *et al.* PEG-modified GoldMag nanoparticles (PGMNs) combined with the magnetic field for local drug delivery. *J. Drug Target.* 19, 161–170 (2011).

32. Kumawat MK, Thakur M, Gurung RB *et al.* Graphene quantum dots for cell proliferation, nucleus imaging, and photoluminescent sensing applications. *Sci. Rep.* 7, 15858 (2017).

33. Li S, Zhou S, Li Y *et al.* Exceptionally high payload of the IR780 iodide on folic acid-functionalized graphene quantum dots for targeted photothermal therapy. *ACS Appl. Mater. Interfaces* 9, 22332–22341 (2017).

• **Shows a good tumor targeting of folic acid-functionalized graphene quantum dots *in vivo*.**

34. Ding H, Zhang F, Zhao C *et al.* Beyond a carrier: graphene quantum dots as a probe for programmatically monitoring anti-cancer drug delivery, release, and response. *ACS Appl. Mater. Interfaces* 9, 27396–27401 (2017).

35. Chen J, Zhang W, Zhang M *et al.* Mn(II) mediated degradation of artemisinin based on Fe_3O_4@MnSiO3-FA nanospheres for cancer therapy *in vivo*. *Nanoscale* 7, 12542–12551 (2015).

36. Li H, Fu C, Miao X *et al.* Multifunctional magnetic co-delivery system coated with polymer mPEG-PLL-FA for nasopharyngeal cancer targeted therapy and MR imaging. *J. Biomater. Appl.* 31, 1169–1181 (2017).

37. Iannazzo D, Ziccarelli I, Pistone A. Graphene quantum dots: multifunctional nanoplatforms for anticancer therapy. *J. Mater. Chem. B* 5, 6471–6489 (2017).

38. Aggarwal P, Hall JB, McLeland CB *et al.* Nanoparticle interaction with plasma proteins as it relates to particle biodistribution, biocompatibility and therapeutic efficacy. *Adv. Drug Deliv. Rev.* 61, 428–437 (2009).

• **Comprehensively analyzes that surface modification of PEG improves biocompatibility of nanomaterials by reducing nonspecific protein adsorption in the blood, preventing flocculation and subsequent complement activation.**

39. van Dam GM, Themelis G, Crane LMA *et al.* Intraoperative tumor-specific fluorescence imaging in ovarian cancer by folate receptor-[alpha] targeting: first in-human results. *Nat. Med.* 17, 1315–1319 (2011).

40. Meier R, Henning TD, Boddington S *et al.* Breast cancers: MR imaging of folate-receptor expression with the folate-specific nanoparticle P1133. *Radiology* 255, 527–535 (2010).

41. Yang Y, He L, Liu Y *et al.* Promising nanocarriers for *PEDF* gene targeting delivery to cervical cancer cells mediated by the over-expressing FRα. *Sci. Rep.* 6, 32427 (2016).

42. Zheng M, Zhao P, Luo Z *et al.* Robust ICG theranostic nanoparticles for folate targeted cancer imaging and highly effective photothermal therapy. *ACS Appl. Mater. Interfaces* 6, 6709–6716 (2014).

43. Nägele H, Castel MA, Deutsch O *et al.* Heart transplantation in a patient with multiple sclerosis and mitoxantrone-induced cardiomyopathy. *J. Heart Lung Transplant.* 23, 641–643 (2004).

44. Safra T, Muggia F, Jeffers S *et al.* PEGgylated liposomal doxorubicin (doxil): reduced clinical cardiotoxicity in patients reaching or exceeding cumulative doses of 500 mg/m^2. *Ann. Oncol.* 11, 1029–1033 (2000).

45. Ramirez LH, Zhao Z, Rougier P *et al.* Pharmacokinetics and antitumor effects of mitoxantrone after intratumoral or intraarterial hepatic administration in rabbits. *Cancer Chemother. Pharmacol.* 37, 371–376 (1996).

46. Chen H, Wang Z, Zong S *et al.* A graphene quantum dot-based FRET system for nuclear-targeted and real-time monitoring of drug delivery. *Nanoscale* 7, 15477–15486 (2015).

47. Dehaini D, Wei X, Fang RH *et al.* Erythrocyte–platelet hybrid membrane coating for enhanced nanoparticle functionalization. *Adv. Mater.* 29, 1606209 (2017).

48. Tian J, Luo Y, Huang L *et al.* PEGylated folate and peptide-decorated graphene oxide nanovehicle for *in vivo* targeted delivery of anticancer drugs and therapeutic self-monitoring. *Biosens. Bioelectron.* 80, 519–524 (2016).

49. Chen W, Ouyang J, Liu H *et al.* Black phosphorus nanosheet-based drug delivery system for synergistic photodynamic/photothermal/chemotherapy of cancer. *Adv. Mater.* 29, 1603864 (2017).

50. Ge J, Lan M, Zhou B *et al.* A graphene quantum dot photodynamic therapy agent with high singlet oxygen generation. *Nat. Commun.* 5, 4596 (2014).

51. Yang X, Wang Y, Huang X *et al.* Multi-functionalized graphene oxide based anticancer drug-carrier with dual-targeting function and pH-sensitivity. *J. Mater. Chem.* 21, 3448–3454 (2011).
52. Fu J, Zhu Y. Lysosomes activating chain reactions against cancer cells with a pH-switched prodrug/procatalyst co-delivery nanosystem. *J. Mater. Chem. B* 5, 996–1004 (2017).
53. Chen Y, Cheng L, Dong Z *et al.* Degradable vanadium disulfide nanostructures with unique optical and magnetic functions for cancer theranostics. *Angew. Chem. Int. Ed. Engl.* 56, 12991–12996 (2017).
54. Conde J, Oliva N, Atilano M *et al.* Self-assembled RNA-triple-helix hydrogel scaffold for microRNA modulation in the tumour microenvironment. *Nat. Mater.* 15, 353–363 (2016).
55. Yang J, Liu X, Bhalla K *et al.* Prevention of apoptosis by Bcl-2: release of cytochrome c from mitochondria blocked. *Science* 275, 1129–1132 (1997).

10.2217/nnm-2018-0378